Astronomy
&
Astrophysics

3D radiation hydrodynamics: Interacting photo-evaporating clumps[*]

A. J. Lim[1],[**] and G. Mellema[2]

[1] Dept. of Physics and Astronomy, University College London, Gower Street, London WC1E 6BT, UK
[2] Sterrewacht Leiden, PO Box 9513, 2300 RA, Leiden, The Netherlands
    e-mail: mellema@strw.leidenuniv.nl

Abstract. We present the results of a new radiation hydrodynamics code called *Maartje*. This code describes the evolution of a flow in three spatial dimensions using an adaptive mesh, and contains a combination of a ray tracer and an atomic physics module to describe the effects of ionizing radiation. The code is parallelized using a custom *threadpool library*. We present an application in which we follow the ionization of two dense spherical clumps which are exposed to an ionizing radiation field from a 50 000 K black body. We study various configurations in which one of the clumps shields the other from the ionizing photons. We find that relatively long-lived filamentary structures with narrow tails are formed. This raises the possibility that cometary knots (such as are found in the Helix Nebula) may be the result of the interaction of an ionizing radiation field with an ensemble of clumps, as opposed to the identification of a single knot with a single clump.

Key words. hydrodynamics – radiative transfer – ISM: kinematics and dynamics – ISM: HII regions – planetary nebulae: general

1. Introduction

The combination of the size of typical astrophysical fluid problems and the capabilities of computers has for decades limited computations to two dimensions. Only in the mid-nineties the first three-dimensional calculations appeared, and slowly three-dimensional fluid calculations are becoming standard. This development has been aided by the increase of processor speed, but also by the development of two techniques: adaptive mesh refinement (AMR) and parallel processing. These two techniques are unrelated, and often even hard to combine, but they both serve to reduce the amount of work a processor needs to do. AMR does this by dynamically concentrating points at locations in the computational mesh which (by some criterion) are considered to be more interesting. In parallel processing the calculation is spread out over several processors, each of which therefore receives a smaller amount of work to do.

A separate trend in astrophysical fluid dynamics has been to combine it with the relevant "microphysics" of the gases under consideration. Interstellar gas tends to emit radiation when heated, photons may heat and ionize the gas, chemical reactions may take place, dust particles may interact with gas particles, etc. Including the effects of magnetic fields could be considered to be part of the same trend, but because the connection between the fields and the flow is more intricate, this is generally considered to be a separate branch of astrophysical fluid dynamics, magnetohydrodynamics (MHD).

In this paper we describe the first results of a new code, named *Maartje*, in which three dimensional hydrodynamics on an adaptive mesh is combined with a simplified photo-ionization calculation. For this calculation one has to follow the progress of ionizing photons on the grid using a radiation transfer routine, which is complicated due to the adapative nature of the grid.

We apply this code to the problem of two photo-evaporating clumps, placed close enough to each other to be able to interact. This problem is a natural extension of the single photo-evaporative clump problem studied in Mellema et al. (1998) which can therefore serve as a comparison. It also has relevance for the system of cometary knots seen in the Helix nebula (O'Dell & Handron 1996; Meaburn et al. 1996) and interacting proplyds in the Orion Nebula (Graham et al. 2002), as well as being a first step towards studying the propagation of ionization fronts through highly inhomogenous media, such as for example happened during the re-ionization of the universe (Shapiro et al. 1998).

The outline of the paper is as follows: in Sect. 2 we describe the different components of the code in some more detail. Section 3 deals with the simulations, from the initial conditions to the interpretation. The conclusions are summarized in Sect. 4.

---

2. A portrait of Maartje

Our aim was to develop a code which could do three-dimensional hydrodynamics (based on the Euler equations), combined with a photo-ionization calculation. For this the following components are needed:

1. An adaptive mesh;
2. A three-dimensional hydrodynamics solver;
3. A "ray tracer" (radiation transfer routine);
4. A microphysics routine (calculating the ionization, heating, and cooling rates);
5. Parallelization.

We have adopted a modular approach to the structure of Maartje, in that each of the components above comprises a separate code "object" (in the non-technical sense of the word), which interacts with the other objects only through interface functions. This allows a remarkable degree of flexibility in the construction of a numerical model. The microphysics calculation is a purely local routine, the three-dimensional hydrodynamics solver and the ray tracer need to interact with the adaptive mesh. We will now describe these components in some detail.

2.1. A three-dimensional hydrodynamics solver

For the three-dimensional hydrodynamics solver we have used a dimensionally split version of the Flux-Vector Splitting (FVS) algorithm (van Leer 1982) to solve the inviscid Euler equations in 3D. This algorithm is known to be stable for high Mach number flows and has been extensively used in astrophysical calculations. The one-dimensional algorithm is extended to three dimensions using a predictor-corrector method: an intermediate state is calculated using the fluxes for all three coordinate directions, and this intermediate state is used to calculate the final fluxes. This makes the method second order accurate in time. Second order accuracy in space is achieved by using linear gradients and a limiter function (Falle 1991).

Many other types of solvers are available (see e.g., Laney 1998), and we have to a large extent "decoupled" the fluid calculation from the other modules of the code, enabling one to choose between a number of fluid-dynamic solvers with little or no re-coding. For example, we have also implemented a Roe solver (Roe 1981; Eulderink & Mellema 1995), and we also made an implementation of the Total Variation Diminishing scheme for MHD of Ryu & Jones (1995). The results in this paper were however, achieved with the FVS scheme.

2.2. An adaptive mesh

The adaptive mesh used in *Maartje* is essentially the *Reefa* linked adaptive mesh described by Lim & Steffen (2001). Some modifications have been made to the adaptive algorithm, notably the refinement now takes place using a "1–to–8" cubic scheme rather than the "8–to–27" scheme described in Lim & Steffen (2001), and in the *Yguazu* code described by Raga et al. (2000). In the 1–to–8 scheme a cubic cell is refined into eight equal parts, meaning that the cell centres in subsequent
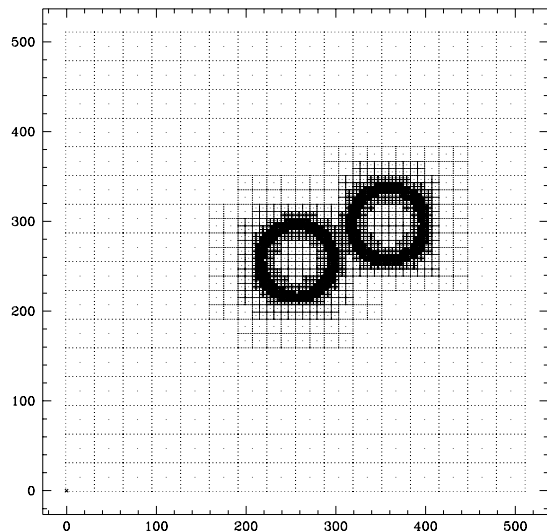

Fig. 1. The mesh refinement for the initial conditions of model I described in Sect. 3.1.

refinement levels are not being spatially coincident, but the cell volumes are. In the 8–to–27 scheme, refinement is performed by adding points in between existing points, meaning that certain points only exist at higher refinement levels, but that volumes defined as having mesh points at their centres, do not overlap. Since the FVS scheme is a finite volume scheme, coincident volumes are preferable.

We do not group refined points into grids, a technique known as "block structuring", used for example in the popular algorithm developed by Berger & Colella (1989). We do require that any refined point only has neighbours which exist on either the same refinement level, or at most one level higher or lower. The refinement criteria are purely based on gradients. A sample of the refinement scheme for the initial state of the two-clump problem we study in Sect. 3 is shown in Fig. 1.

2.3. A ray tracer

In order to follow the transfer of ionizing photons on the grid we have to collect column densities of photon absorbing species. In the current version the only photon-absorber is neutral hydrogen and the relevant atomic physics is described below. The problem of describing numerically the interaction of a radiation field with a fluid flow is a non-local one. Radiation may transport (photon) energy from any region to any other, depending on the local atomic processes and on the geometry of the density field between these regions. We have included in *Maartje* two ray tracing modules each using a different method to determine the radiation field;

i) The "Short Characteristic" Tracer. This method is based upon an interpolation technique in which the column density from a source cell is determined over the entire grid via a cell-by-cell method. First one can find the column density in cells adjacent to the source cell and, by interpolation, in those cells which share a vertex with the source cell. The same technique is then used to find the column density in cells adjacent to all cells with known column densities, etc., until the column density
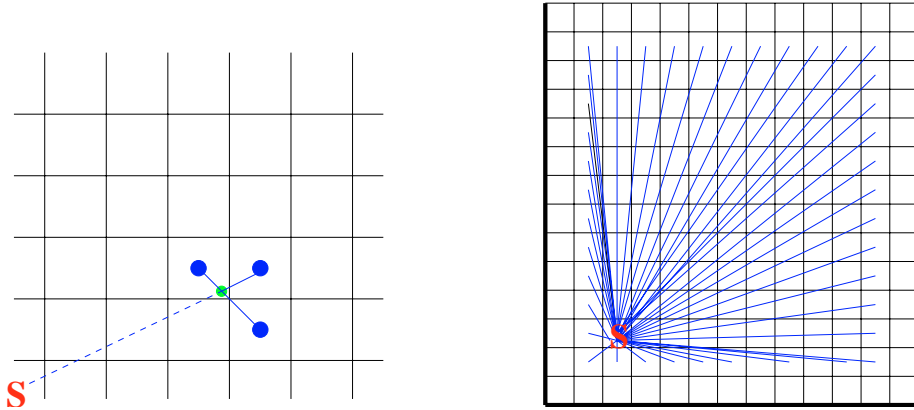
Fig. 2. Schematic overview of the short and long characteristic methods. The point marked "S" is the source point.

from the source cell is known over the entire grid. This method is described in more detail in Raga et al. (1999).

ii) The "Long Characteristic" Tracer. An alternative method is to calculate the exact path of the ray from the source cell to the destination cell. This is accomplished by calculating (from simple geometry) the entry and exit points of the ray from all cells between the source and destination. This yields the column density from the source to the destination, and also a matrix of path data comprised of the path length, intensity and physical conditions in all cells along the ray path. For problems with more complex radiative transfer than we consider, the path matrix can be passed to a dedicated line radiation transport solver. A review and bench-marked comparison of such solvers is presented in van Zadelhoff et al. (2002).

It is also possible to develop a technique whereby the long characteristic tracer is used in reverse to calculate the effect of many sources upon a single destination cell, allowing a self-consistent computation of the diffuse field due to emission both from other regions of the grid and from putative off-grid sources.

Maartje is also capable of including the parallel-integrated chemistry module described by Lim et al. (2001), which will be needed for complex molecular line transport.

2.4. A microphysics routine

For the calculation of the local ionization/recombination rates, as well as heating and cooling rates, we use a simplified version of the *DORIC* routines. This approach is described in Raga et al. (1997) and Mellema et al. (1998). Those implementations contained an extensive list of species, here we limit ourselves to hydrogen only, and use a cooling curve for the radiative cooling. For hydrogen we determine the collisional and photo-ionization rates, and the recombination rate (case B) to calculate the time-dependent ionization state. For the thermal state of the gas we calculate the heating through photo-ionization and cooling due to radiative losses and collisional ionization.

For the photo-ionization rate and the heating rate due to photo-ionization, we need to evaluate integrals over the spectral energy distribution of the ionizing source, attenuated by the optical depth. Instead of evaluating these integrals when calculating the rates, we calculate a table of integral values for a range of (logarithmically spaced) optical depths at the H ionization threshold. During the calculation we find the rates by interpolation in these tables, using the local optical depth at $h\nu = 13.6$ eV. This procedure is described in detail in Frank & Mellema (1994).

For the cooling rate we use the cooling curve from Dalgarno & McCray (1972), $\Lambda(T)$. The local radiative cooling rate is then given by $n^2\Lambda(T)$, with n the particle number density.

These microphysics routines are simplified, but for the problem at hand they suffice. We find that the evaporation time for a single clump is for instance not substantially different from the one found using the more sophisticated version of *DORIC* (Mellema et al. 1998). Since the microphysics routine is a module, it is in fact not very hard to substitute it for something more advanced.

2.5. Parallelization

Current techniques for the parallelization tend to rely on the use of precompiled libraries, such as MPI or OpenMP. The former library does not support so-called shared memory, and is typically suited for codes in which whole meshes can be calculated by one processor, which is not the case for *Maartje*. OpenMP is typically used in combination with an "auto-parallelization" library with which one can instruct the compiler to parallelize given loops within the program.

Given the very different types of calculation described above, all of which would ideally operate in parallel, we consider the OpenMP approach to be somewhat inflexible. In addition many of the algorithms we use are recursive rather than loop-based in nature. We have therefore developed a custom parallelization library (based on ANSI standard POSIX threads) which, rather than parallelize on a loop basis, simply receives pointers to i) a function to be executed and ii) a data-structure containing the arguments to that function. The function is then executed within a separate thread of control on an available processor. Parallelization can then be implemented at the code level rather than the compiler level. Using this approach, all of the above modules operate in a multi-processor fashion on a shared memory machine. The radiative transfer is parallelized per source point. For the short characteristic tracer

we need the column density at every point for every source point. This makes is necessary to store the column densities for every source point being worked on, hence involving memory overhead.

3. Test: Self-shielding photo-evaporating clumps

As a demonstration of the capabilities of *Maartje*, we chose to apply it to the calculation of the photo-evaporation of two dense clumps, in different configurations. Before presenting those results, we first examine the photo-evaporation of a single clump.

3.1. Comparison with Mellema et al. (1998)

Mellema et al. (1998) studied the photo-evaporation of a single dense clump in two dimensions, assuming axi-symmetry. In order to test Maartje, we ran the same problem in three dimensions.

The clump has an initial density of 5000 cm^{-3}, a temperature of 100 K and a radius of 10^{16} cm. The clump is embedded in an ionized environment with a density of 100 nuclei cm^{-3} and a temperature of 5000 K. In order to reduce spurious flows which can arise from artificial stepwise boundaries we have softened the outer 5% of the clump with a linear fall-off to the environmental density. This clump is exposed to the radiation from a star with a black-body spectrum of effective temperature 50 000 K and luminosity 7000 $L_\odot$, thus producing 4.8×10^{47} ionizing photons per second. Placing the star at a distance of 10^{18} cm from the left x-face of the grid, we can assume that the incident radiation is plane parallel. Treating each cell on the $x = 0$ face of the grid as a source from which we calculate column densities, for rays travelling parallel to the x-axis, the short and long characteristic tracers become identical.

In all of the models presented here we use an adaptive mesh with four levels of binary refinement, maximum resolution 512 cells in each coordinate direction. The grid is a cube with a physical size of 2.048×10^{17} cm in all directions. Free-flow boundary conditions are imposed on all faces of the grid.

We chose a larger grid than Mellema et al. (1998), so that the photo-evaporative flow does not cross the boundaries early during the simulation. Subsonic flows crossing a free-flow boundary may affect the flow inside the grid, which is best avoided.

We find that the clump evolves in a similar way as described in Mellema et al. (1998): first it gets compressed as a shock wave induced by the ionization front travels into it. Once this shock wave has travelled through the entire clump, it acquires a cometary shape, and starts to accelerate. In Fig. 3 we show the neutral clump mass as a function of time, and compare it to the result from Mellema et al. (1998). As one can see, the match is not perfect, but still quite close. We did find that the result of both the 2D and 3D simulations depend on the choice of the timestep, or on how often the radiative transfer is done. The variation in the total evaporation time is about 15%. The results of Mellema et al. (1998) were achieved by only doing the radiative transfer every 5 time steps. We applied the radiative effects every time step, but chose the time step to stay close to the 2D results. Since the solution found by
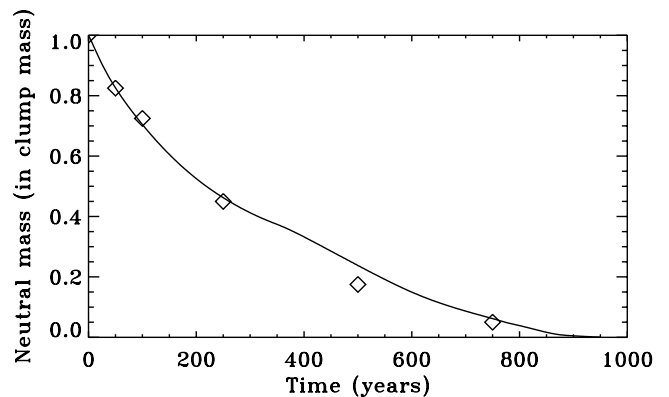

Fig. 3. Graph of the neutral clump mass against time. The solid line shows the results for the 3D simulation, the symbols are values from the 2D simulation in Mellema et al. (1998).

Table 1. Clump centre positions[1].

Model	Clump A	Clump B	Position angle
1	$(0, -1)$	$(0, 1)$	0°
2	$(-1, 0)$	$(1, 0)$	90°
3	$(-1, -0.5)$	$(1, 0.5)$	63°
4	$(-1.5, -0.5)$	$(1.5, 0.5)$	72°

[1] In units of 10^{16} cm.

Mellema et al. (1998) was found to nearly reproduce the analytic solution, this provides to good baseline for studying the problem of two interacting photo-evaporative clumps.

3.2. Initial and boundary conditions

For the simulations with two clumps, we used the same properties as listed above for the single clump. We ran four simulations, numbered 1 through 4, in each of which the two clumps are oriented differently with respect to one another. We will refer to the occulting clump as A and the occulted clump as B. The clump centres are always placed in the central z-plane of the grid and their $[x, y]$ coordinates vary. The $[x, y]$ coordinates of the clumps (relative to the central point of the grid) in models 1 to 4 are listed in Table 1.

Models 1 and 2 start with the clumps arranged parallel and perpendicular to the impinging radiation field, respectively. In model 1, both clumps are exposed to the full radiation field with no initial shadowing, in model 2, clump A completely eclipses clump B at the start of the simulation. In models 3 and 4 clump B is partly in the shadow of clump A, having only 39.1% ($2/3 - \sqrt{3}/(2\pi)$) of its cross-sectional area eclipsed by the shadow of clump A.

3.3. Results

The results of the four simulations illustrate the two ways in which the clumps can affect each other. First, there is the occultation which produces an asymmetric ionization front in the
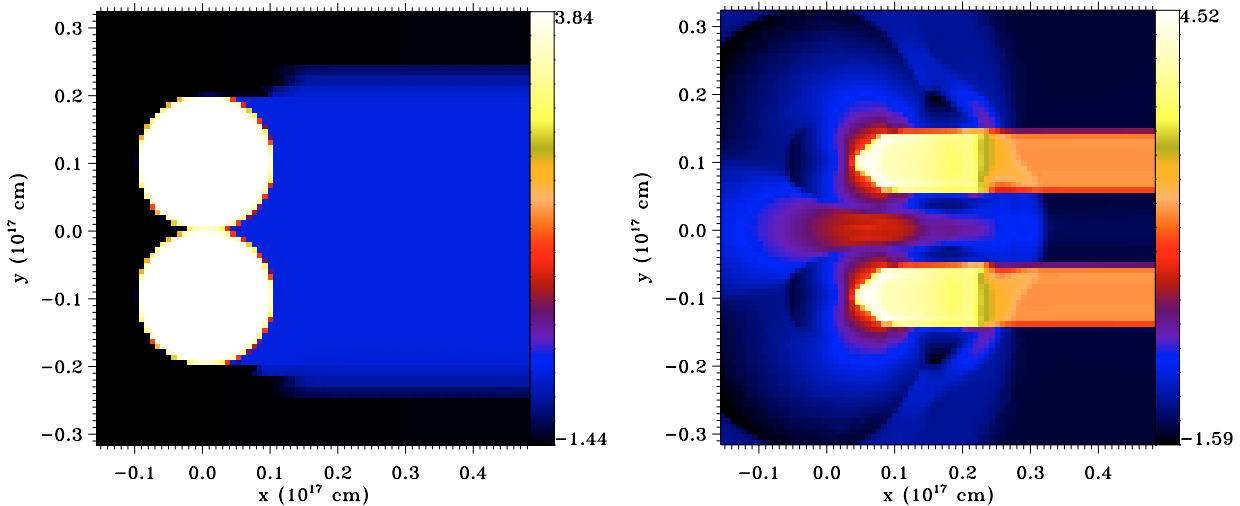
Fig. 4. Colour plots of $\log_{10}$ of the number density (cm^{-3}) from run 1 at times 0 (left) and 500 years (right), in the $z = 1.024 \times 10^{17}$ cm plane. Only a fraction of the computational domain is shown. The coordinates are centred on the centre of the grid.

clump B. Second, there are the photo-evaporative flows, which interact with each other, and in some cases with the clumps themselves. Even though we use a simple configuration, the resulting flow patterns quickly become complex. For lack of space, we can only present some snapshots of the simulations. Movies of all four cases can be found with the electronic version of this paper.

3.3.1. Interaction of photo-evaporative flows

In model 1 there is no occultation of either clump, and hence the only interaction is through the photo-evaporative flows, see Fig. 4. These collide in the midplane of both clumps. Since the two evaporative flows carry the same momentum flux, and the clump centres are aligned perpendicular to the incoming photon flux, the interaction zone lies exactly in the middle between the clumps. A photo-evaporative flow is driven by the pressure at the ionization front, and this pressure is mostly a function of the incoming ionizing flux. From Bertoldi & McKee (1990), Eq. (3.23), it can be seen that the photo-evaporative pressure is approximately given by

$$\frac{p_c}{k} = 2.45 \times 10^7 \sqrt{\frac{S_{49}}{r_{c,pc} R_{pc}^2}} \text{ cm}^{-3} \text{ K}, \qquad (1)$$

in which S_{49} is ionizing photon rate in units of 10^{49} s^{-1}, R_{pc} the distance to the ionizing source, and $r_{c,pc}$ the radius of the cloud, both in parsecs. This value is only weakly dependent on the cloud radius, and for small clouds this dependence actually becomes even weaker. Therefore the evaporative flows of clouds of similar size will always be approximately balanced.

Apart from the sheet created by the two photo-evaporative flows, the evolution of the two clumps proceeds exactly as in the single clump case.

In the other simulations interaction of photo-evaporative flows also occur. However, since these flows are also balanced, the photo-evaporative flow from one clump cannot typically

reach the other clump. The only effect is then to create a collision zone where the two evaporative flows meet.

3.3.2. Occultation

The effects of occultation are much more intricate. In simulation 2, one clump is completely in the shadow of the other, see Fig. 5. However, as the first clump starts to shrink due to the shock front travelling into it, photons manage to reach the surface of the second clump, ionizing it in a cylindrical fashion, and only slowly, due to the low impact angle. Once the first clump has been completely shocked, it starts moving due to the rocket-effect, and collides with the second clump, compressing its front side. Since it has been shocked and therefore has a higher density, clump A actually manages to drill through clump B, creating a cylindrical, photo-evaporating shell.

Occultation is thus found to have two major effects: asymmetric ionization of the second cloud, and collision between the first cloud and the occulted part of the second cloud. The latter effect will be larger when the clouds are near one another. The sequence of images showing central cuts of the density for simulation 3 illustrates the chain of events, see Fig. 6. One sees how clump B only gets ionized on the side where the direct photons can penetrate. This creates a photo-evaporation flow which also impacts on the occulted part of the clump, and drives a shock wave into it. As the shock-wave driven by the D-type ionization front moves through clump B, the occulted and unocculted parts start to separate. Once the shock has moved through the entire unocculted part, it starts to move, and then evolves as a photo-evaporating clump in the cometary phase. The occulted part is shocked and acquires a velocity perpendicular to the incoming radiation field, moving it further into the shadow of clump A. As the first clump starts moving, it collides with the remnant of clump B, and they merge to form a slightly larger cometary knot, which finally completely evaporates.

During this later phase, the tail of clump A to a large extent consists of material from clump B, making this another
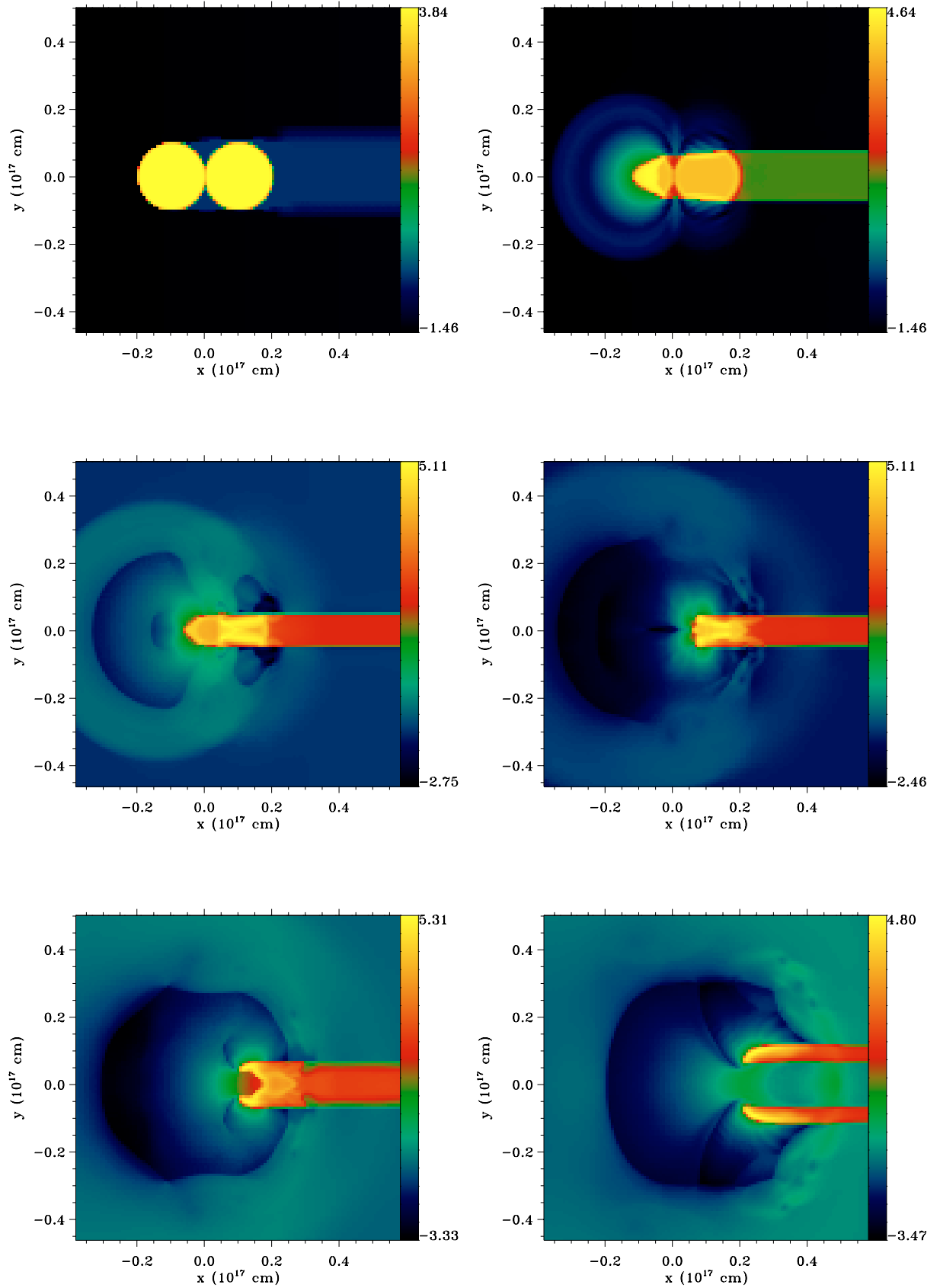
Fig. 5. Colour plots of $\log_{10}$ of the number density (cm^{-3}) from run 2 at times 0 (top left), 250, 500, 750, 1000 and 1500 years (bottom right), in the $z = 1.024 \times 10^{17}$ cm plane. Only a fraction of the computational domain is shown. The coordinates are centred on the centre of the grid.
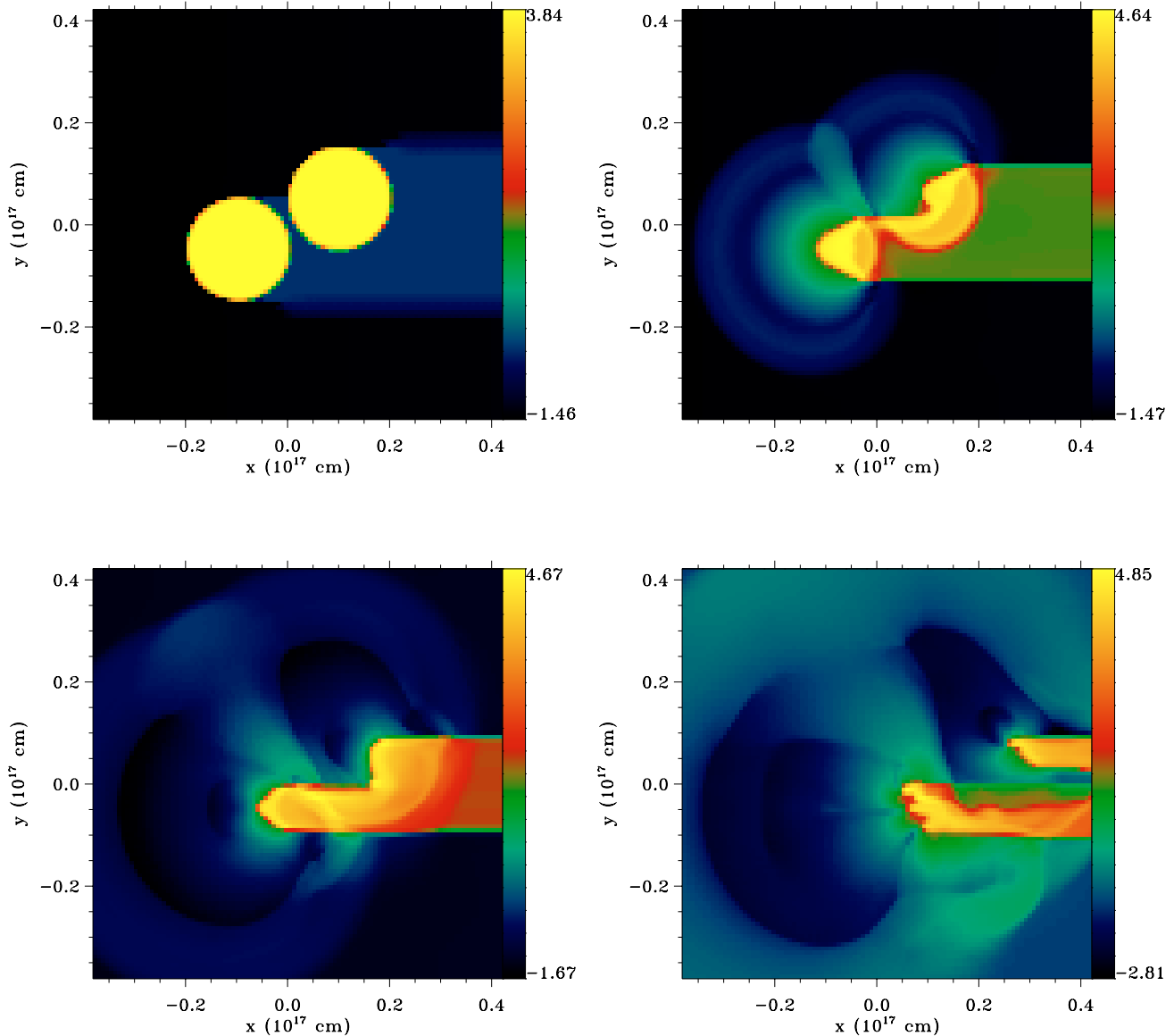
Fig. 6. Colour plots of $\log_{10}$ of the number density (cm^{-3}) from run 3 at $t = 0$ (top left), 250 (top right), 500 (bottom left), and 750 years (bottom right), in the $z = 1.024 \times 10^{17}$ cm plane. Only a fraction of the computational domain is shown. The coordinates are centred on the centre of the grid.

mechanism to form tails behind photo-evaporating clumps (cf. Dyson et al. 1993; Cantó et al. 1998).

For the merging of two clumps to be possible, the second clump should be within the evaporation distance of the first clump, x_{evap}. For this one can use the expression given in Mellema et al. (1998), Eq. (49). This may be re-expressed as a filling factor. The volume in which the second clump has to be is given by $\pi r_c^2 x_{evap}$, or rather less than this, since r_c is getting smaller with time. Assuming a linear decrease of r_c with time, the cone shaped volume is $\frac{1}{3}\pi r_c^2 x_{evap}$. To have part of another clump of radius r_c overlap with this volume, we need a clump density of $1/(\frac{7}{3}\pi r_c^2 x_{evap})$. For a density of clumps n_c, each with volume V_c, the filling factor is giving by $f = V_c n_c$, which means that the required filling factor is given by $f = \frac{4}{7} r_c / x_{evap}$. For our typical clumps, $x_{evap} \approx 5 r_c$, so that we need approximately a 10% filling factor.

In Fig. 8 we show evaporation graphs for the four simulations. The graphs show the amount of neutral clump material, relative to the amount of initial clump material. Comparing to the single clump curve, one sees how the occultation typically prolongs the lifetime of the neutral phase by between 30 and 50%, depending on the configuration.

The evaporation curves of models 3 and 4 differ only in the later stages of the calculation. The reason for this is as follows: If there is a filling factor of zero then the evaporation time of the two clumps will be fixed and roughly independent of the distance between the clumps. However, if there is a finite filling factor, the clumps will merge at some point. Prior to this point the photo-evaporation will proceed roughly as if the clumps were far apart, but when the clumps merge they have a relative velocity parallel to the radiation field. This will result in a "splattering" of the clump material which increases the
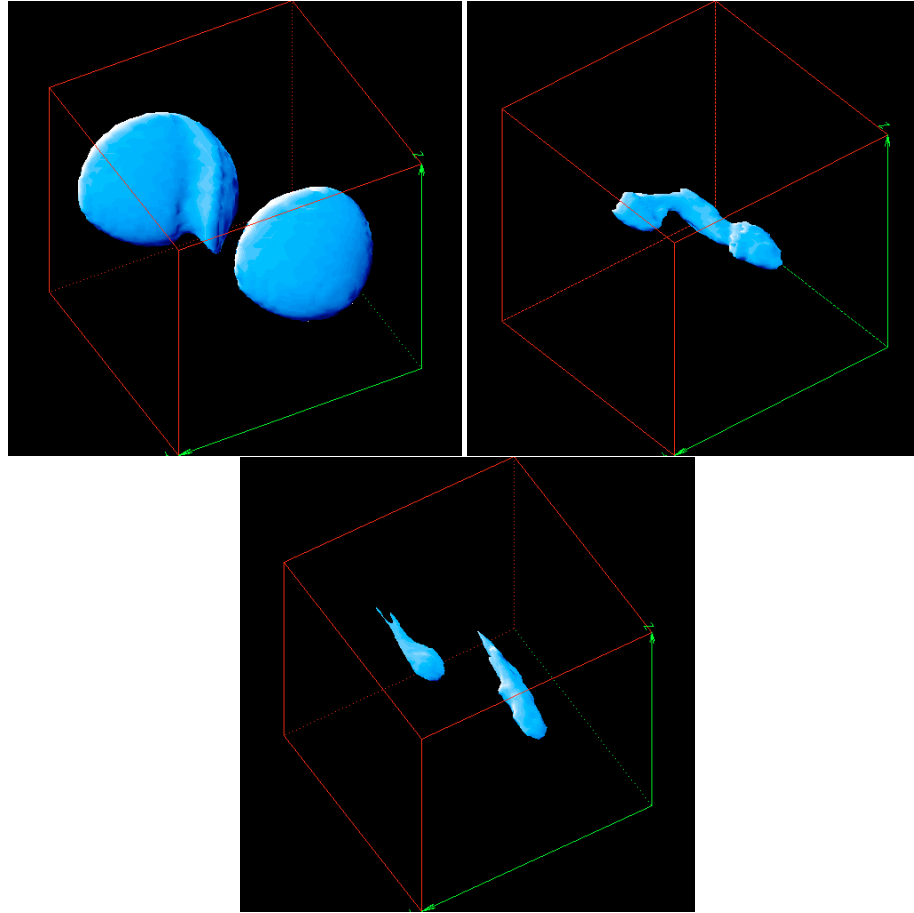
Fig. 7. Isodensity surface plot of the number density from run 3 at t = 250 (top left), 500 (top right), and 750 years (bottom). Compare with Fig. 6.
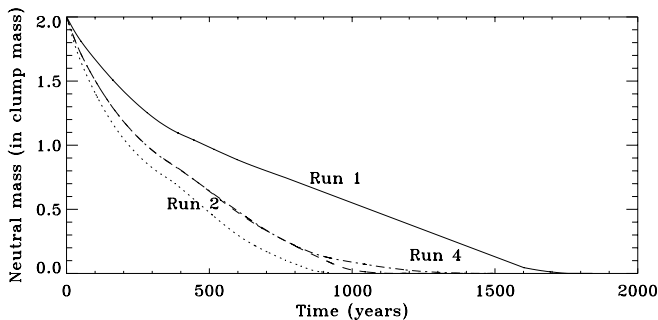

Fig. 8. Graph of the neutral clump mass against time for the four runs. The graph for run 3 is the dashed line.

surface area exposed to the ionizing radiation and thus decreases the lifetime of the merged object. In model 4 the clumps are further apart than in model 3, therefore this collision and splattering occurs later and the effects are seen as an increase in the lifetime of the neutral component in model 4.

4. Comparison to observations

There are not many situations in which one observes photo-evaporating clumps directly. The clearest example are the cometary knots (CKs) in the Helix Nebula, NGC 7293 (O'Dell & Handron 1996; Meaburn et al. 1996). A number of the CKs

show indication for interaction with their neighbours, but it is hard to make any quantitative comparison between the models and the observations. If merging took place, this could explain the presence of dust in the tails of the CKs, which would be hard to form if the tails were the product of accretion from the environment, as in the model of Cantó et al. (1998). Note that the general effects of occultation are quite noticeable as the CKs and also the proplyds in the Orion nebula produce observable shadow regions (O'Dell 2000).

Graham et al. (2002) report the detection of two interacting proplyds in the Orion nebula. They deduce the existence of an interaction zone due to the two photo-evaporating flows. Occultation does not appear to play a role in this system. As discussed above, these authors also find that the photo-evaporative flows are closely matched in momentum flux, and form a sheet in between the two proplyds. We find similar sheets in our simulations, although of smaller size because of the chosen configurations.

In Fig. 9 we show maps of the calculated Hα emission from both recombination and collisional excitation for run 3, as seen from the three main coordinate directions. The clumps are assumed to be optically thin for the Hα photons. One can recognize the classical cometary shapes and how at early times, the clump B is already notably deformed. The front view shows ring-like features due to the fact that the path length through
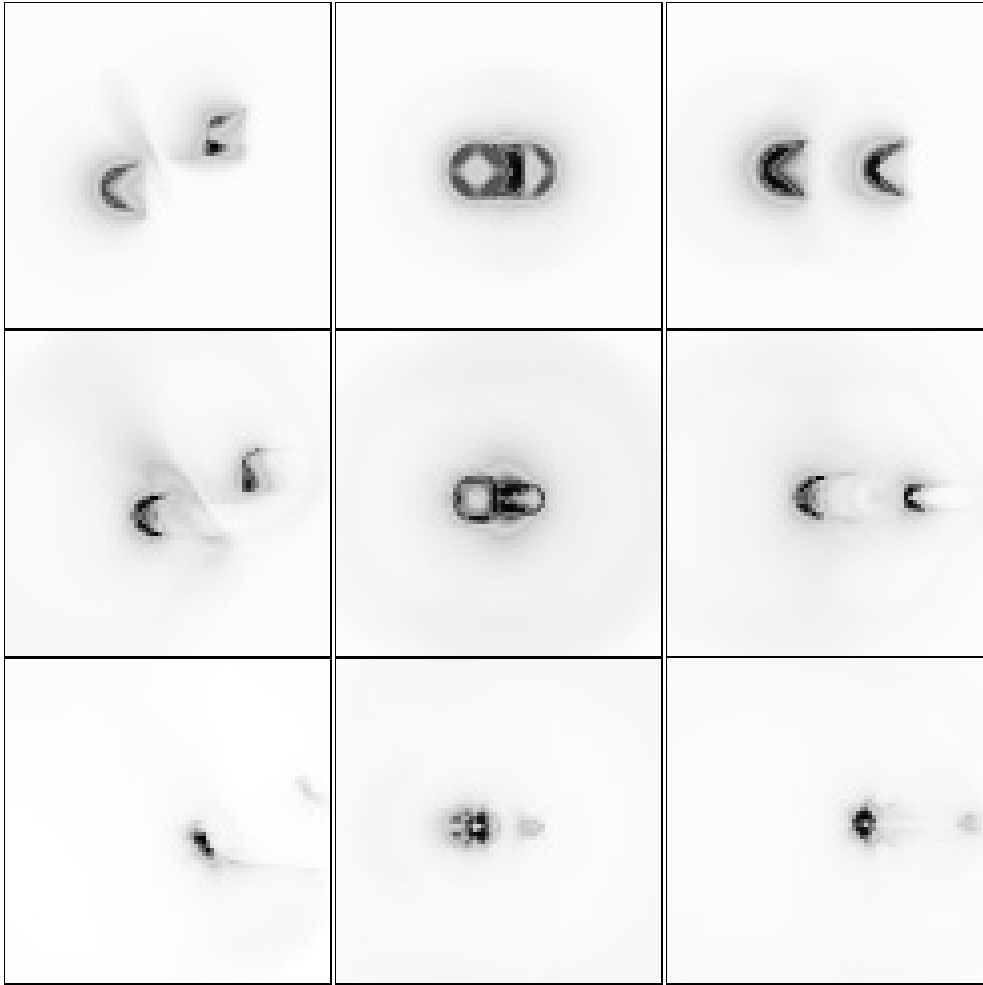
Fig. 9. Synthesized Hα emission line images at times $t = 250$ (top row), 500 (middle row), and 750 years (bottom row), as they would be observed from three different directions: along the z-axis, x-axis, and y-axis (from left to right).

the wings of the comet is much larger than through the centre. In the side view, the interaction region can be seen, and also the photo-evaporative flow can be observed as faint haloes around the two clumps.

5. Conclusions

We showed that it is possible to combine an adaptive mesh refinement algorithm with a ray tracing algorithm to do a combined hydrodynamic and radiative transfer calculation in three spatial dimensions. We applied this method to the problem of a set of photo-evaporating clouds, using different configurations to illustrate how these clouds can interact with each other.

We find that the complex interaction can be attributed to two main effects, the interaction of the photo-evaporative flows and occultation. The photo-evaporative flows (because of their origin) are expected to be fairly balanced in momenta, and will therefore never reach the photo-evaporating surface of a neighbouring clump. The occultation of clumps by each other can lead to merging of clumps. Since the photo-evaporative flow is perpendicular to the clump surface the occulted clump acquires a velocity which drives it into the shadow of the occulting clump. This increases the efficiency of merging. It is

conceivable that observed photo-evaporating clumps (such as the Cometary Knots seen in the Helix Nebula) are the result of merging. This would explain the fact that dust is found to be present in the tails. Merging requires initial filling factors of around 10%.

In general the survival time of the neutral components increases by approximately 30% due to the occultation. This should be generally true for a layer of clumps with covering factor (as seen from the source of ionizing photons) of 1.

We plan to use *Maartje* for further studies of dynamic photo-ionization processes, such as "methode champenoise" flows in star formation regions, or the overlap of different HII regions.

References

Berger, M. J., & Colella, P. 1989, J. Comp. Phys., 82, 64

Bertoldi, F., & McKee, C. F. 1990, ApJ, 354, 529

Cantó, J., Raga, A., Steffen, W., & Shapiro, P. 1998, ApJ, 502, 695

Dalgarno, A., & McCray, R. A. 1972, ARA&A, 10, 375

Dyson, J. E., Hartquist, T. W., & Biro, S. 1993, MNRAS, 261, 430

Eulderink, F., & Mellema, G. 1995, A&AS, 110, 587

Falle, S. A. E. G. 1991, MNRAS, 250, 581

Frank, A., & Mellema, G. 1994, A&A, 289, 937

Graham, M. F., Meaburn, J., Garrington, S. T., et al. 2002, ApJ, 570, 222

Laney, C. 1998, Computational Gasdynamics (Cambridge: Cambridge University Press)

Lim, A. J., Rawling, J. M. C., & Williams, D. A. 2001, A&A, 376, 336

Lim, A. J., & Steffen, W. 2001, MNRAS, 322, 166

Meaburn, J., Clayton, C. A., Bryce, M., & Walsh, J. R. 1996, MNRAS, 281, L57

Mellema, G., Raga, A. C., Cantó, J., et al. 1998, A&A, 331, 335

O'Dell, C. R. 2000, AJ, 119, 2311

O'Dell, C. R., & Handron, K. D. 1996, AJ, 111, 1630

Raga, A. C., Mellema, G., Arthur, S. J., et al. 1999, Rev. Mex. Astron. Astrofis., 35, 123

Raga, A. C., Mellema, G., & Lundqvist, P. 1997, ApJS, 109, 517

Raga, A. C., Navarro-González, R., & Villagrán-Muniz, M. 2000, Rev. Mex. Astron. Astrofis., 36, 67

Roe, P. 1981, J. Comp. Phys., 43, 357

Ryu, D., & Jones, T. W. 1995, ApJ, 442, 228

Shapiro, P. R., Raga, A. C., & Mellema, G. 1998, Mem. Soc. Astron. It., 69, 463

van Leer, B. 1982, in Lecture Notes in Physics, vol. 170, Eight International Conf. of Numerical Methods in Fluid Dynamics, ed. E. Krause (Berlin: Springer Verlag), 507

van Zadelhoff, G.-J., Dullemond, C. P., van der Tak, F. F. S., et al. 2002, A&A, 395, 373